Chapter 5
In-situ and Kinetic Studies Using Neutrons

Götz Eckold and Helmut Schober

Abstract Neutrons provide unique possibilities for in-situ studies of condensed matter due to their ability to penetrate large samples and work pieces, to distinguish between neighboring elements and even between isotopes of the same element, to interact with magnetic moments and to map nuclear and magnetic excitations. The range of applications extends from biological or soft matter systems over basic superconducting and magnetic investigations to all kinds of materials science under a great variety of external conditions. Complex and sophisticated sample environments have been developed in the past to study samples under external perturbations and extreme conditions like high or low temperatures, high pressures and mechanical stresses, electric and magnetic fields and different kinds of chemical environments. Not only equilibrium studies are in the focus of neutron scattering investigations—increasing interest in real-time kinetic studies lead to new techniques that allow even inelastic studies on time scales down to the microsecond regime thus providing most direct information about the changing chemical bonds in materials. In the present chapter, we want to provide an overview over recent developments for in-situ studies using neutrons and to highlight some application in materials science without having the ambition to give a comprehensive review. Selected examples of neutron studies under extreme conditions from a variety of different disciplines are collected to demonstrate the power of neutron scattering for materials characterization. Moreover, kinetic studies providing information about the relaxation behavior of materials under external load are presented covering time-scales

---

G. Eckold (✉)
Institut für Physikalische Chemie, Georg-August-Universität Göttingen, Tammannstrasse 6,
37077 Göttingen, Germany
e-mail: geckold@gwdg.de

H. Schober
Science division, Institut Laue-Langevin, 6, rue Jules Horowitz, BP 156,
38042 Grenoble Cedex 9, France
e-mail: schober@ill.eu

A. Ziegler et al. (eds.), *In-situ Materials Characterization*,
Springer Series in Materials Science 193, DOI: 10.1007/978-3-642-45152-2_5,

from hours or days down to the microsecond regime. Those investigations are the basis for the understanding of the basic microscopic mechanisms and allow one to tailor materials using non-equilibrium states.

5.1 Introduction

Neutron scattering has become a standard tool for investigating condensed matter. Like any scattering technique it extracts information about the structure and dynamics of the sample from the momentum and energy distribution of the scattered particle. The neutron interacts with the nuclei and magnetic moments present in a material. This interaction has exactly the right strength for the investigation of bulk samples. As a rule of thumb, we aim for a scattering probability in the 10 % range. This value assures that we have on one hand a sufficiently intense scattered signal and that on the other hand only a small fraction of that signal originates from multiple scattering. Multiple scattering is detrimental to the data analysis as it destroys the correspondence of momentum (Q) and energy (E) change connected with a single scattering event on one side and the detectable overall energy and momentum change on the other side. For a thermal neutron beam 10 % of scattering corresponds in the case of Aluminium to passing through one billion layers of atoms or about 1 cm of sample. In the case of hydrogenated samples this thickness has to be reduced by about a factor 100 but remains a fraction of a mm. The weak scattering power combined with generally weak absorption leads to a high penetration power of neutrons. This allows for a straightforward use of even complex and bulky sample environment. The low absorption has the additional benefit of depositing little energy per unit volume of sample. Thermal neutrons contrary to intense X-ray beams thus constitute a delicate probe of matter that is adapted even to fragile materials.

The energies of neutron beams that are available for materials research range from a few neVs up to eVs. The corresponding neutron wavelengths cover the full range from the sub-atomic (fractions of an Å) to the super-molecular spacing (several nm). Thus while the wavelengths are comparable to those of X-rays the energies are orders of magnitude smaller. This is due to the fact that the neutrons have been thermalized in the moderators of the neutron sources and hence possess energies corresponding to the moderator temperatures. As a consequence, neutron energies match the typical energies of excitations at these temperatures. This facilitates dynamic studies, as the energy exchanged with the sample is generally a good fraction of the initial energy of the neutron. Neutrons thus provide access to the slow motion of polymers as well as the fast excitations in the electronic spin system.

A particularity of neutrons is the fact that they interact with the nuclei and are, therefore, sensitive to isotopes. As isotopes have little influence on the chemistry this sensitivity can be exploited for contrast variation. The most prominent example is the total or partial substitution of hydrogen by deuterium. This so-called deuteration is at the very heart of many investigations in the fields of

Table 5.1 Characteristic performance parameters of neutrons

Size and sensitivity	Time scales
Smallest sample volume 0.001 mm^3	Shortest time detectable 10^{-15} s
Sensitivity to displacements 10^{-4} nm	Longest relaxation times meas. 10^{-6} s
Chemical sensitivity 10 ppm	Time resolution for kinetics $<10^{-3}$ s
Magnetic sensitivity 0.01 μB/atom	Stability in time: years

soft condensed matter and biology. The coupling of the spin of the neutron to microscopic magnetic fields makes the neutron a unique probe to decrypt even the most complex magnetic structures and fluctuations.

There has lately been a strong boost in performance mainly due to instrument upgrades enabled by new technology. These upgrades lead to an increased sensitivity of the spectrometers. It is now possible to investigate samples as small as 0.001 mm^3 (for other performance parameters see Table 5.1). The increased flux is particularly useful when it comes to kinetic studies that are the subject of this article.

Modern materials investigations require sophisticated sample environment. It is important that the microscopic picture given by the neutron scattering experiment reflects the properties of the sample under well-defined conditions. While the in-situ study of systems under extreme conditions like temperatures in the nano-Kelvin regime or above 2000 K, pressures of several 100 GPa, magnetic fields in the 20 T-regime or electric fields of several 10 kV/cm provide new information about the properties of materials in thermodynamic equilibrium, time-resolved investigations allow monitoring the evolution of a system towards equilibrium. If a system is exposed to a sufficiently strong external perturbation, the reaction path can be tracked by microscopic methods like diffraction or scattering. Quite frequently, intermediate states are detected that are meta-stable in character but exhibit unusual and exciting properties. If required these intermediate states can be stabilized over large time-intervals by appropriate (thermal) treatments like quenching thus leading to new non-equilibrium materials.

In the following, we want to illustrate the possibilities of neutron techniques for the characterisation of transition states and kinetic behaviour. It is not the aim of this article to provide a comprehensive review of kinetic studies with neutrons. Rather, we want to highlight recent developments in this field using some selected examples.

There are two fundamentally different kinds of kinetic studies: Single shot experiments, on the one hand, are usually restricted to processes or reactions that occur on time-scales adapted to the counting times of neutron experiments, i.e. seconds to hours. With stroboscopic experiments, on the other hand, one can access much shorter time scales down to the microsecond regime at least, but these studies are restricted to repeatable processes and can also be considered as pump-and-probe experiments.

The unique property of the neutron as a strongly penetrating probe allows using sophisticated sample environments to produce the required perturbations of the system from equilibrium. More precisely, extreme conditions of temperature, pressure or stress, electric and magnetic fields as well as chemical potential can be realized—and this not only statically, but also in a cyclic way that allows for stroboscopic measurements.

5.2 Conditions Available for In-situ Studies

The main aim of this article is to give insight into the possibilities of investigation that neutrons offer for kinetic studies. Before doing so we would like to review briefly the conditions available for in-situ studies in general. Whether these conditions can be applied to kinetic studies will then depend as outlined above on the counting-times and possibilities of cycling.

5.2.1 Temperature

Using standard techniques, temperatures between a few mK and 1500 K are easily accessible at almost every type of neutron instrument, from diffractometers over small angle instruments to spectrometers. There are, however, dedicated developments for experiments of lowest temperatures down to the nanokelvin range, which is particularly interesting for the investigation of small magnetic interactions leading e.g. to the ordering of nuclear spins. One of the main activities in this lowest temperature science with neutrons is concentrated at the BER-II research reactor in Berlin [1].

On the other extreme, new devices are being developed that allow performing neutron scattering experiments on large samples at temperatures well above 2500 K. Particularly promising are acoustic or electromagnetic levitation techniques that allow for measurements without containers [2–4].

Subjects of investigation are the structure and dynamics of liquids and melts as well as anharmonic effects or disorder phenomena in high-temperature materials.

5.2.2 Pressure and Stress

Hydrostatic pressures up to 1 GPa are routinely available on nearly all instruments. This value is small compared to the pressures available with diamond-anvil cells at X-ray facilities. The difference is explained by the larger samples needed for neutron experiments. The so-called Paris-Edinburgh-cell was developed to meet the requirement of large volume while considerably extending the pressure range. Pressures up to 10 GPa at sample volumes of 100 mm^3 and temperatures from 80 to 1000 K can thus be realised in routine operation [5–8]. The application of hydrostatic pressure is of particular interest for geological applications. Moreover, the origin of negative thermal expansion of materials can also be studied by high-pressure inelastic work since the variation of phonon frequencies with pressure determines the Grüneisen-parameters.

High-pressure work has been identified as a very important and growing field of neutron science. In the US, the Los Alamos Neutron Science Centre LANSCE has made great efforts to provide specialised devices for the use with different neutron instruments [9]. At the FRM II in Garching, a multi-anvil press is being installed at the new time-of-flight diffractometer. This huge device will enable experiments und geologically relevant conditions, i.e. pressures up to 25 GPa and temperatures up to 2800 K for sample volumes of 20 mm^3. Moreover, The multi-anvil design allows one to perform dedicated deformation experiments since all anvils can be individually driven.

Another kind of in-situ experiments under mechanical load at stationary conditions are rheological studies on soft matter with small angle neutron scattering. Stationary shear stresses can be applied by rotating cups in the Couette configuration or by using a plate–plate geometry, e.g., in order to investigate the structural changes of polymers, micellar solutions or gels. A dedicated Neutron Rheometer for high torques up to 200 Nm or high shear rates up to 865 s^{-1} has been commissioned at the Los Alamos Science Centre recently [10]. For high-viscosity systems a rheometer using rotating plates was installed at the ISIS Spallation Source at Rutherford Appleton Laboratory [11].

Externally applied stress is equally a very important parameter in classical materials engineering investigations. During the past decade, diffractometers dedicated to the determination of stress from the measurement of lattice strain have been developed which can host complete mechanical components or structures. They enable in-situ studies for the determination of materials properties, manufacturing parameters or in service behavior, simulating real operational conditions. By measuring the strain response as a function of applied stress the (diffraction) elastic constants of a material can be determined. These parameters are vital for the calculation of stresses from lattice strain measurements. In the same manner, in-situ deformation studies of materials can be performed. Since diffraction is crystal orientation and phase selective, the study of deformation mechanisms and load sharing in single phase, multiphase or composite materials is possible. Other important investigations performed are on crack development, creep or fatigue behavior of a material by applying constant or cyclic loading during a diffraction experiment [12–14].

Additionally, investigating phase fractions, stress and texture during processes such as welding is a challenging experimental work, since an automated welding bench has to be operated on the diffractometer. However initial in-situ studies have already been performed on fusion and friction welding during neutron diffraction experiments [15].

5.2.3 Magnetic Fields

Cryomagnets with split coil geometry are frequently used for neutron scattering experiments. The combination of strong fields and very low temperatures allows the study of magnetic ordering phenomena and details of complex magnetic interactions. The simultaneous use of polarized neutrons provides even more information. Nowadays, magnets with fields up to 7–10 T belong to the standard equipment of modern neutron facilities and even 15 T-split coil magnets are available.

To go beyond these field strengths requires extremely great efforts since the design of those magnets always has to provide enough space for incoming and scattered neutrons, thus leading to enormous forces between the pole shoes. Currently, a high-field magnet is going to be installed at the neutron source BER II of the Helmholtz-Zentrum Berlin at a dedicated instrument for extreme environments ExED [16]. It is expected that continuous fields above 30 T can be realised that allow entering new scientific areas such as the investigation of the fractional quantum Hall effect. In combination with the time-of-flight neutron instrument, both elastic and inelastic experiments under those extreme conditions will be feasible.

It is a lot easier to produce pulsed fields. The difficulty of using these devices for neutrons is related to the total counting statistics. The integrated acquisition time for a given field strength is limited by the pulse duration and the number of repetitions. It has only recently been demonstrated that despite these limitations neutron diffraction patterns can be obtained with pulsed magnetic fields up to 30 T [17].

5.2.4 Electric Fields

High electric fields are comparatively simple to realise for the investigation of structural and dynamical properties of ferroelectrics, piezoelectrics, multiferroics etc. The maximum field strength usually depends on the sample itself since defects or irregular shape may cause electrical breakdown. Since the sample volume must be sufficiently large in order to yield enough counting statistics, the field are usually limited to some 10 kV/cm. In contrast to X-ray scattering experiments, the electrodes itself are almost transparent for neutrons and provide no severe problems.

5.2.5 Chemical Potential: Partial Pressure

Studies of non-stochiometric systems like oxides in solid oxide fuel cells, in mixed valence systems or other oxygen conductors require the control of the oxygen partial pressure in order to avoid changing concentrations [18]. Moreover, chemical loading of zeolites, hydrogen loading of energy materials, gas adsorption, or the investigation of catalytic reaction on surfaces needs well defined in-situ gas handling systems in order to obtain reliable results. At the Helmholtz Centre Berlin a dedicated gas-handling system was installed that can be used for experiments at different neutron instruments [19]. This equipment opens new fields of chemical applications, in particular.

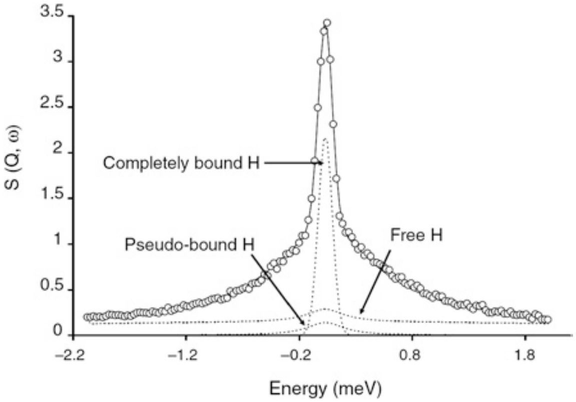

Fig. 5.1 Quasielastic scattering from hydrogen during the hydration of cement [20]

5.3 Single-Shot Kinetic Experiments

We will in the following give a few examples of single-shot experiments. In a pump-probe configuration the evolution of the sample is monitored after an initial perturbation. Quenching or fast heating is frequently used to initiate transitions to a not-equilibrium state of matter. Neutron scattering then allows following the relaxation of this state. In the case of a chemical reaction the initial state is a complex function of reactants and reaction conditions.

5.3.1 Cement Hydration

One important example that has been extensively studied by time-resolved neutron scattering is the hydration of cement. The extraordinary strong incoherent scattering cross section of hydrogen allows studying the single particle motion of hydrogen in great detail. The form of the quasielastic scattering from hydrogen provides direct information about its mobility. As shown by Peterson [20], the scattering profile consists of several distinguishable components reflecting the different mobility of free and bound water. An example is displayed in Fig. 5.1.

Free water exhibits a large diffusivity and, hence, a broad quasi-elastic spectrum while bound water is much less mobile and leads to a narrow and almost elastic component. Quantitative interpretation of those data yields the so-called bound water index BWI that can be used to describe the hydration process. It could be shown, that the time-evolution of the BWI depends on the polymorph of tricalcium silicate that is used. Figure 5.2 shows that the diffusion-controlled hydration is more pronounced in the monoclinic modification resulting in a considerably larger product formation [20, 21].

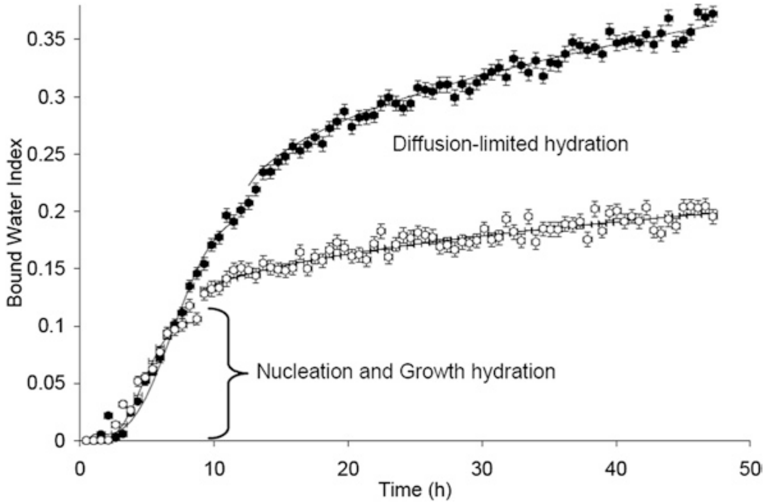

Fig. 5.2 The time-evolution of the BWI for triclinic T_1 (*lower curve*) and monoclinic M_3 (*upper curve*) forms of tricalcium silicate, shown as points with standard deviation. The combined modified Avrami-type nucleation and growth and Fujii and Kondo-derived diffusion-limited models are shown as bold lines [21]

Different kinetic models have been applied to describe the kinetic behaviour quantitatively and, hence the underlying mechanism could be elucidated. Details of the data treatment can be found in [21] or [22]. Additives such as NaOH, $CaCl_2$ or sucrose are found to have a considerable influence on the formation of reaction products [23, 24]. $CaCl_2$, in particular, enhances the hydration of cement as demonstrated by the strong increase of the narrow quasi-elastic component associated with bound water.

The formation of $Ca(OH)_2$ during the hydration reaction of cement can also be monitored by the phonon density of states. Due to the large incoherent scattering cross section of hydrogen, the lattice vibration become more and more visible the larger the $Ca(OH)_2$-content.

5.3.2 Transition Between Ice-Phases

Ice is one of the most fascinating systems offering a wealth of structural features including amorphous and crystalline phases. It is the flexibility of the hydrogen-bond network interconnecting the water molecules that allows for this structural variety. While it is well known that the normal phase of ice exhibits hexagonal symmetry (Ih), up to now fifteen stable and metastable crystalline structures have been observed with interesting kinetic properties. The new high-pressure phase called ice XV has been detected at low temperature only quite recently

Fig. 5.3 Phase diagram of water [25]

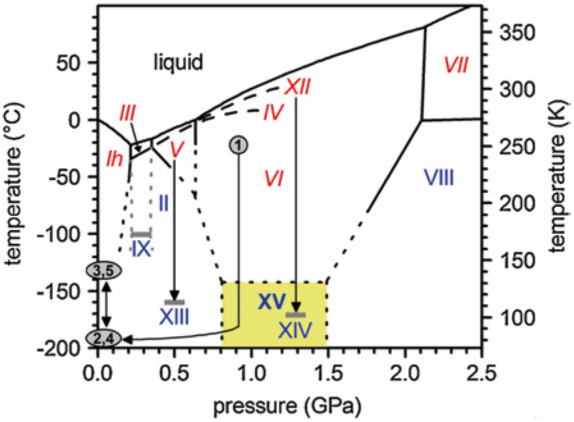

[25]. In Fig. 5.3, the phase diagram of the known crystalline phases is displayed. Neutron diffraction is particularly suited for elucidating the structural details as well as the transitions and, hence, a good number of neutron-related publications are dealing with the study of the water phase diagram as a function of temperature and pressure.

In a recent investigation, Hansen et al. could demonstrate that cubic ice Ic is formed if recovered high-pressure phases of ice IX or ice V are annealed at temperatures near 145 K [26]. Careful Rietveld refinement of the diffraction data allowed performing a quantitative phase analysis. It is shown that the formation of cubic ice takes some hours to proceed. Being metastable, the cubic phase is subsequently transformed into hexagonal ice on heating. The corresponding time-evolution of the stacking sequence could be determined in detail. Figure 5.4 shows the variation of stacking probabilities during the transition from cubic to hexagonal ice.

In addition to the crystalline ice forms, several amorphous phases with different densities are observed. Due to the rather small difference in the chemical potential of these phases, the kinetics of the transition between them is often rather sluggish. Koza et al. give a review about the transformations between different amorphous structures of deuterated ice [27]. As an example, Fig. 5.5 shows the time-evolution of the neutron diffraction pattern during the transition from high- to low-density amorphous ice.

The broad patterns are characteristic for non-crystalline structures and the shift of the intensity maxima to smaller scattering vectors Q directly reflects the decrease of the packing density of the water molecules. It is also seen from Fig. 5.5 that there is a transient increase in intensity at small Q. Small angle scattering experiments helped to study this feature in more detail (see Fig. 5.6).

Obviously, the scattered intensity near 0.1 Å^{-1} initially starts to increase (upper part of the figure) reaching a maximum and finally decreases towards the final state (lower part). In contrast to this finding, the intensity of the very low-Q regime decreases monotonically in time. This so-called Porod-regime is reflecting the grain

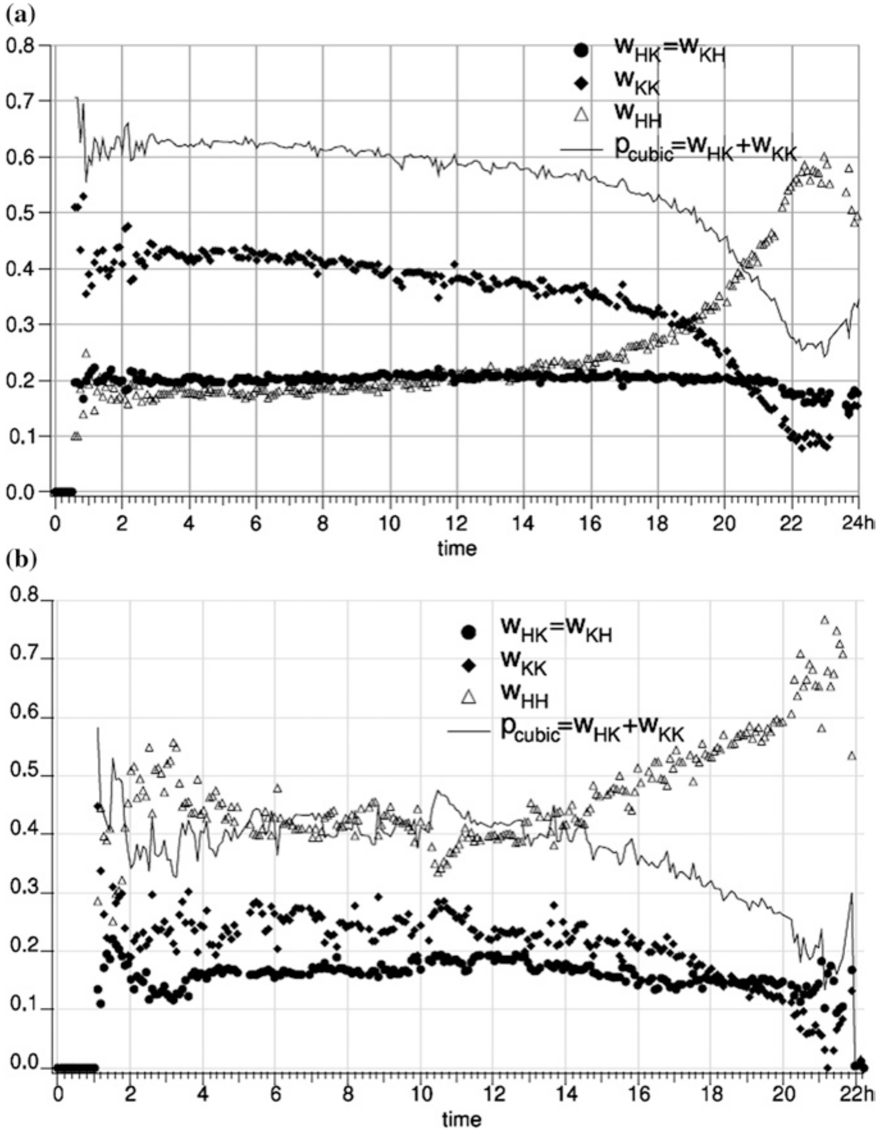

Fig. 5.4 Evolution of the proportion of cubic stacking sequences over time ($w_{HK} + w_{KK}$), of the probability of finding pairs of similar stacking (w_{KK} and w_{HH}) and of interfaces between different stacking types (w_{HH}) for ice Ic as produced from ice V (**a**) and ice IX (**b**) [26]

structure of the sample, while the intermediate regime provides information about the heterogeneity of the sample. On the basis of these observations it is claimed that the transition between the amorphous ice phases occurs on two different timescales: The formation of an intermediate structure characterized by a strong heterogeneity is rather sluggish and depends on the history and the preparation of the

Fig. 5.5 Time evolution of the neutron diffraction pattern during the transition from high to low density amorphous ice [27]

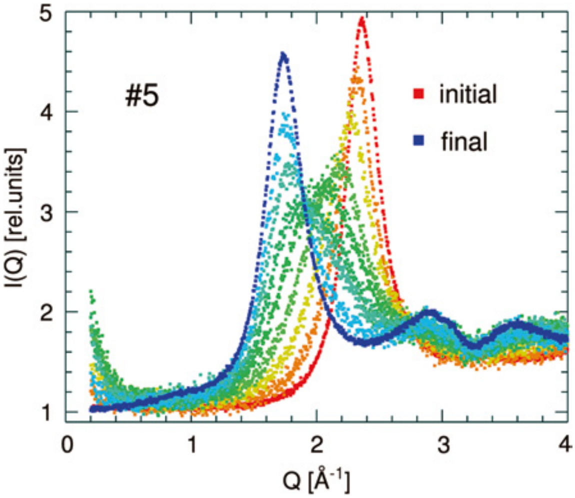

Fig. 5.6 Evolution of the small angle intensity during the transformation from high- to low-density amorphous ice [27]

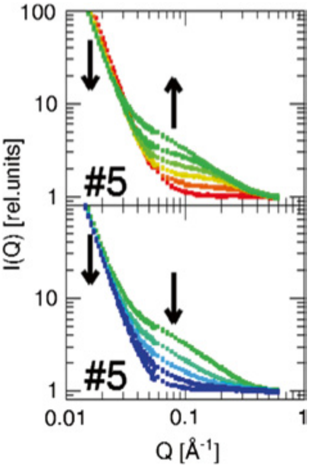

sample under consideration. Typical time scales are of the order of 100 min. The subsequent step of creating a homogenous low-density state is much faster and completed after several minutes for each of the different samples investigated.

5.3.3 *Crystallization of Glass-Phases*

Another actual topic of kinetic studies using neutrons is the crystallization of glass phases upon annealing. Recently, Ma et al. could show that time-resolved diffraction on a time scale of minutes allows extracting the evolution of the atomic

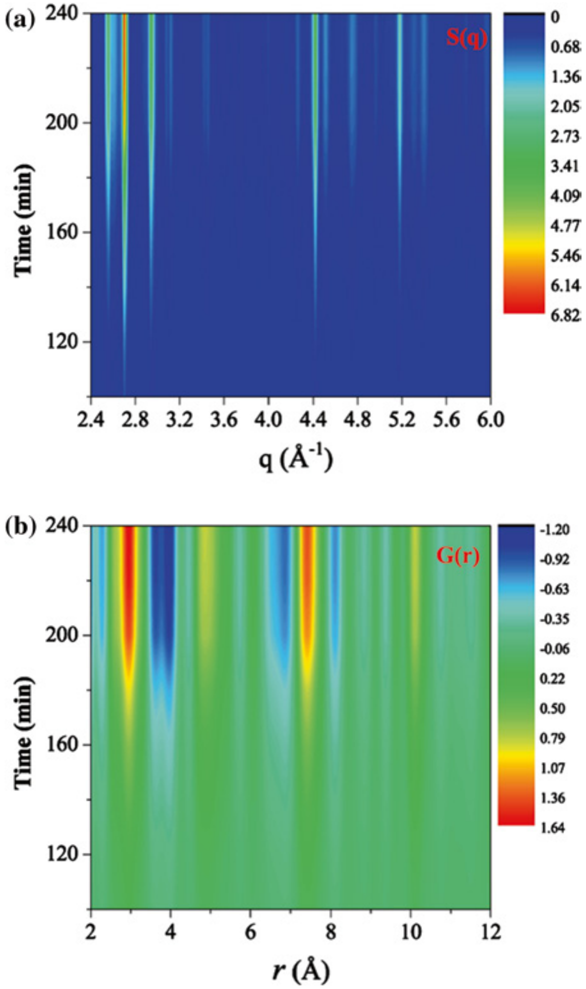

Fig. 5.7 Time evolution of the total structure factor S(q) (*top*) and its Fourier transform, the pair distribution function G(r) (*bottom*) during the crystallization reaction of $Zr_{50.4}Cu_{40.6}Al_9$ metallic glass at 420 °C [28]

pair distribution function for a Zr-based metallic glass [28]. The upper part of Fig. 5.7 shows the time evolution of the diffraction pattern. While at the beginning the characteristic diffuse scattering of the glass phase is hardly seen in this contour plot, the appearance of well-defined Bragg reflections of the crystalline phase dominates the intensity map after about 2 h. From the Fourier-analysis of these data, the time-dependence of the pair distribution function is obtained as shown in the lower part of Fig. 5.7, which illustrates impressively the evolution of the ordered structure.

The quantitative interpretation of the experimental results allows extracting the time dependence of the crystalline volume fraction. It could be shown that this quantity is well described by a stretched exponential function according to the Johnson–Mehl–Avrami model. It is inferred that the underlying process is interface-controlled.

5.3.4 Crystallization Reactions and Extreme Conditions

Reactions under hydrothermal conditions require a sophisticated sample environment. Recently, first results with a newly designed hydrothermal cell developed at the Australian Nuclear Science and Technology Organisation ANSTO for use with the powder diffractometer WOMBAT have been published by Xia et al. [29]. Due to the fact that a Ti-Zr alloys with zero coherent scattering length has been used as cell-material excellent background conditions could be achieved. At the same time, a stainless-steel mesh supporting the sample serves as an internal standard. One of the first applications of this cell addressed the kinetics of the transformation from leucite ($KAlSi_2O_6$) to analcime ($NaAlSi_2O_6 \cdot H_2O$) as an example of pseudomorphic transformations, Fig. 5.8.

It was known that under hydrothermal conditions leucite is dissolved in an aqueous NaCl-solution followed by the precipitation of analcime and the overall reaction can be summarized as

$$KAlSi_2O_6 + Na^+ + H_2O \rightarrow NaAlSi_2O_6 \cdot H_2O + K^+.$$

The time scale of this process was, however, unknown. The time-evolution of the corresponding diffraction pattern at 210 °C is shown in Fig. 5.8. The individual peaks can be well assigned to the different phases and a Rietveld-least squares fitting procedure yields the time-dependence of the respective mass fractions. These data are displayed in Fig. 5.9 and can be well described by an Avrami-equation with an exponent of 2.

5.3.5 Self-Assembly in Soft Matter

Processes of self-assembly in soft matter systems can be well monitored by real-time small angle neutron scattering since the scattering contrast can be adjusted by selective deuteration of one component. An illustrative example is the pressure-induced reorganisation of micellar solutions. In aqueous solution, surfactant molecules of tetradecyl-trimethylammonium-bromide (TTAB) are forming almost spherical micelles as long as the critical micelle concentration (cmc) of 3.8 mM is exceeded. The self-organisation of these particles is reflected by a correlation peak at wave vector transfers close to 0.05 Å^{-1} as shown in Fig. 5.10a [30] for a 25 mM solution of TTAB. Using specific models one is able to extract not only the geometrical parameters of the micelles but also their charges.

If pressure is applied to this system, only minor structural changes are observed up to 1000 bar and can be attributed to the compressibility of the solvent (D_2O). After increasing the pressure to 1100 bar, however, the scattered intensity drops dramatically on a time scale of hours due to the beginning crystallization of the system and the formation of so-called hydrated crystals as illustrated by the sequence of scattering profiles in Fig. 5.10b.

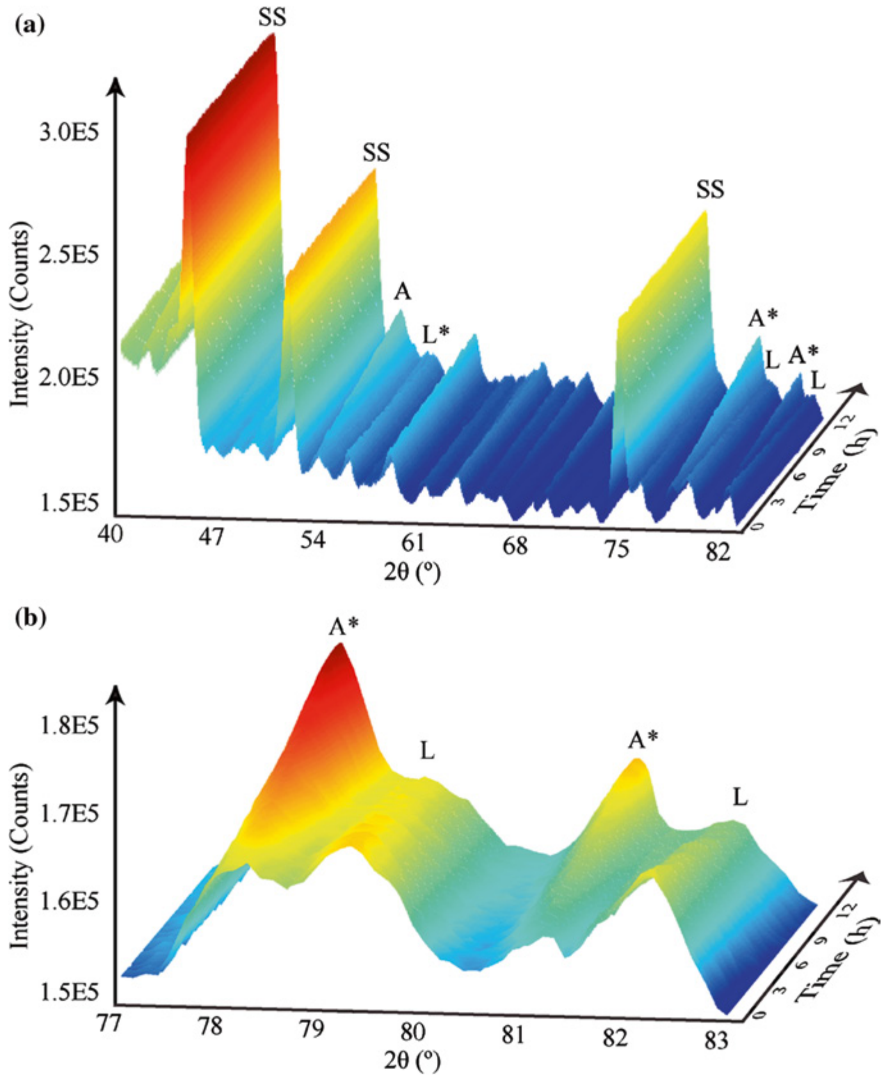

Fig. 5.8 In-situ neutron diffraction patterns of the transformation from leucite ($KAlSi_2O_6$) to analcime ($NaAlSi_2O_6{\cdot}H_2O$). **a** Two-theta range from 40° to 83°, showing the progressive phase transformation. **b** Two-theta range from 77° to 83°, highlighting the progressive increase of analcime peaks and decrease of leucite peaks. *L* leucite peaks, *A* analcime peaks, *L**(*A**) overlapped peaks where leucite (analcime) is the dominant phase, *SS* stainless steel peaks [29]

This simple behaviour changes drastically if the concentration is increased to, say, 360 mM. Here, the transition starts at smaller pressures but it is not completed any more. Rather, the time-resolved experiments show that even after long periods of time a considerable part of the correlation peak, which is a signature of the liquid micellar phase, remains detectable and a new equilibrium

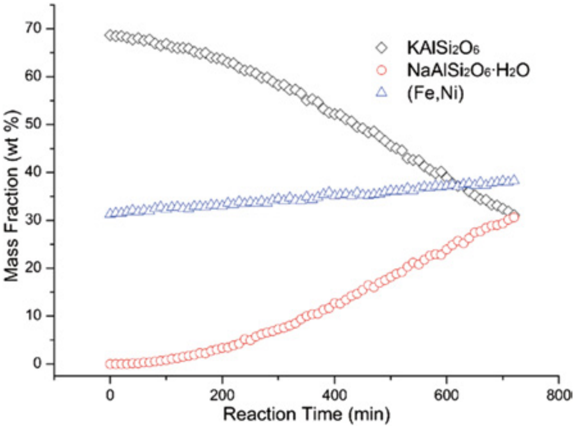

Fig. 5.9 Mass fractions of the three involved phases as a function of reaction time during the transformation from leucite ($KAlSi_2O_6$) to analcime ($NaAlSi_2O_6·H_2O$) [29]. Note that the total mass of the sample changed from 1.25 g at the beginning of the reaction to 0.92 g at the end because of the loss of small particles from the mesh tube; however, the mass of the stainless steel mesh tube remained constant at 0.57 g, so the mass fraction of (Fe,Ni) slightly increased during the process, serving as an excellent internal standard for quantification

state is formed. For a 360 mM solution of TTAB in D_2O the time evolution of the small angle scattering intensity after applying a hydrostatic pressure of 700 bar is displayed in Fig. 5.11.

The correlation peak shifts towards smaller scattering angles and simultaneously the intensity decreases. The time-dependence of the integrated intensity (Porod-invariant) is shown in the inset along with the behaviour at 900 bar. Due to the larger thermodynamic driving force at higher pressures the kinetics become faster and the residual intensity corresponding to the remaining liquid micellar phase becomes smaller. In a pressure-concentration phase diagram, a two-phase regime develops towards higher concentrations where the solid and the liquid micellar phase coexist.

Due to the sluggish kinetics of the underlying process a careful determination of the phase diagram needs the time-resolved data in order to extrapolate the saturation value of the intensity.

While in this system, the correlation peak in the small angle regime is the characteristic feature for the (homogeneous) micellar solution, which is reduced by the fractional crystallization, the reverse feature, the growth of the intensity maximum is frequently observed, if inhomogeneous structures are formed by demixing reactions.

Exchange reactions of single surfactant molecules between micelles and the solution can be studied using the unique possibility of contrast variation by deuteration. Lund has shown that block-co-polymer micelles built from poly(ethylene-propylene) PEP and poly(ethylene oxide) PEO in water or water dimethylformamide (DMF) mixtures exhibit a complex kinetic behaviour [31]. The exchange of individual molecules between different micelles was monitored

Fig. 5.10 **a** Small angle scattering from 25 mM TTAB-solution at 25 °C at different pressures. **b** Time evolution of scattering profiles at 1100 bar (in the inset the time dependence of the Porod invariant is shown). Note, that the individual curves are shifted vertically for clarity [30]

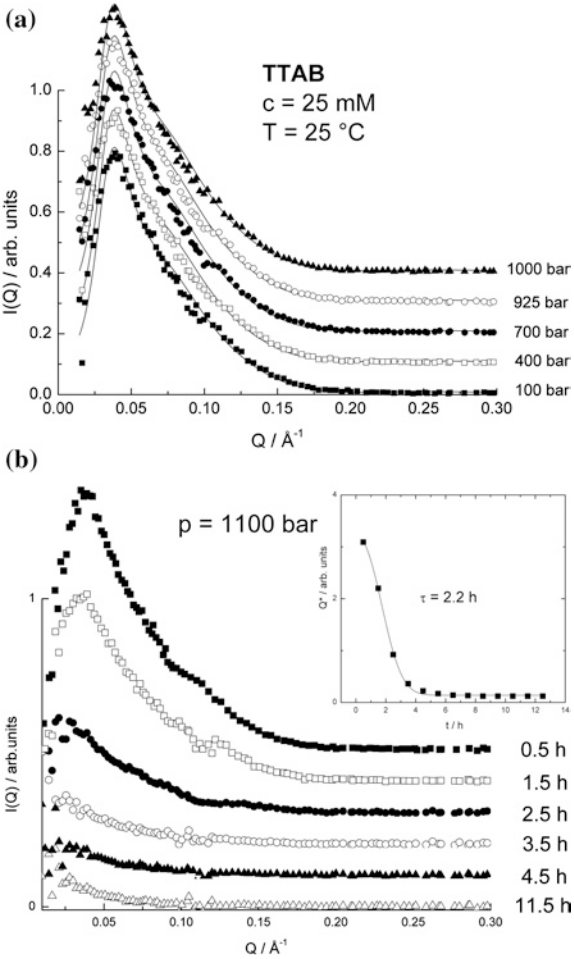

by mixing deuterated and hydrogenated polymers. The solvent was chosen to yield just the same scattering length density as a micelle that consists of a random mixture of both types of polymers. Hence, those micelles are invisible in small angle neutron scattering experiments. If, however, the micelles consist exclusively of deuterated or hydrogenated polymers the scattering contrast with respect to the solvent is large and the size and the shape of micelles, e.g., can be determined with accuracy from the scattering profiles. In a kinetic experiment, Lund et al. have prepared both types of micelles separately. After mixing both systems individual polymer molecules may leave one micelle and migrate to another, thus leading to a more random isotope distribution. Hence, the scattered intensity will decrease in time and the rate of the exchange reaction can be determined [32].

Using pure water as solvent, no exchange reaction was observed over hours. Adding dimethyl-formamide, however, leads to a significant reduction of

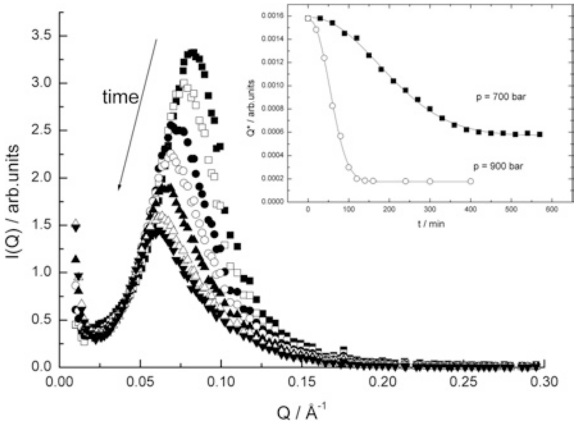

Fig. 5.11 Time evolution of SANS intensity of 360 mM TTAB solution at 25 °C and 700 bar. In the inset, the time dependence of the Porod invariant is shown—for comparison the data for 900 bar are also included [30]

the interfacial tension and, consequently, also to an increased expulsion and exchange rate of polymers from and between the micelles. The corresponding relaxation function, i.e. the square root of the normalized intensity, is shown in Fig. 5.12 for a system of PEP1-PEO20 micelles with a volume fraction of 1 % in a 25 % DMF-water mixture at different temperatures. It can be seen that the kinetics is much more complicated than expected from the simple theory of Halperin and Alexander [33] that predicts a simple exponential decay. It could be excluded that the deviations are due to polydispersity. Rather, the data suggest that only part of the polymer molecules are able to escape rapidly from the micelle—these are molecules that are located close to the interface and have a compact conformation. Other molecules in the interior of the micelle suffer from topological interactions with the surrounding polymers and dynamic constraints that lead to a much slower exchange kinetics. Therefore a broad range of relaxation times may be expected that leads to the kinetic behaviour as reflected by Fig. 5.12.

Small angle neutron scattering is also suitable for the study of the formation and growth of larger aggregates like vesicles. Grillo et al. [34] have investigated the transformation from micelles to vesicles of sodium bis(2-ethyl hexyl)sulfosuccinate (AOT) induced by the addition of salts. Using a stopped flow apparatus, the time-evolution of the small angle intensity profile could be observed from 0.5 s up to several hours after mixing. The results are shown in Fig. 5.13. Quantitative interpretation of the data in terms of the structure factors of vesicles allows extracting the time-dependence of the vesicle radius.

As demonstrated by the log–log plot in Fig. 5.14 the radius grows as a power law with an exponent of 1/6, and this over more than four decades in time. This finding indicates that the aggregation rate is essentially determined by the diffusion of micelles that are incorporated within already existing vesicles.

On an even larger length scale the gelation of milk has recently been studied by spin-echo and ultra small angle scattering (SESANS and USANS) [35]. The formation of yogurt from milk can be described as an aggregation process

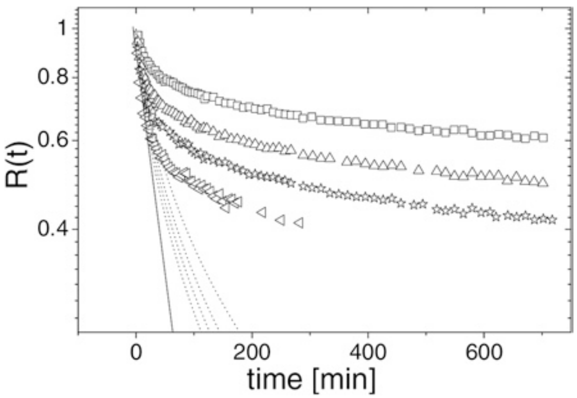

Fig. 5.12 Relaxation kinetics of the PEP1-PEO20 micelles in a 25 mol % DMF/water mixture system at a total volume fraction of 1 % and different temperatures in a semi-logarithmical presentation. From *top to bottom*: 47, 55, 60, and 65 °C. The *solid line* displays the theoretically expected single exponential decay. The *dotted lines* indicate the expected theoretical decay taking into account the polydispersity of the core blocks [32]

Fig. 5.13 Time evolution of small angle scattering intensity after mixing a 0.75 wt. % AOT-solution with 0.042 M NaCl [34]

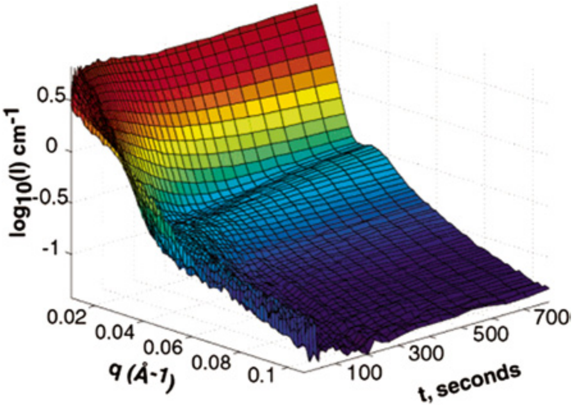

of casein-micelles under the influence of bacteria, increased acidity etc., thus creating a 3D network with increasing length scales. In concentrated real systems, the evolution of these structures cannot be observed by light-scattering or microscopy, since they are in general opaque. Hence, small angle neutron scattering is the method of choice for a detailed study of the structural properties. Advanced techniques like spin-scho small angle neutron scattering SESANS or ultra small angle neutron scattering USANS are, however, needed in order to access characteristic length scales of the order of several 100 nm. Figure 5.15 shows that on a time scale of hours the gelation takes place leading to a network of μm-sized structures.

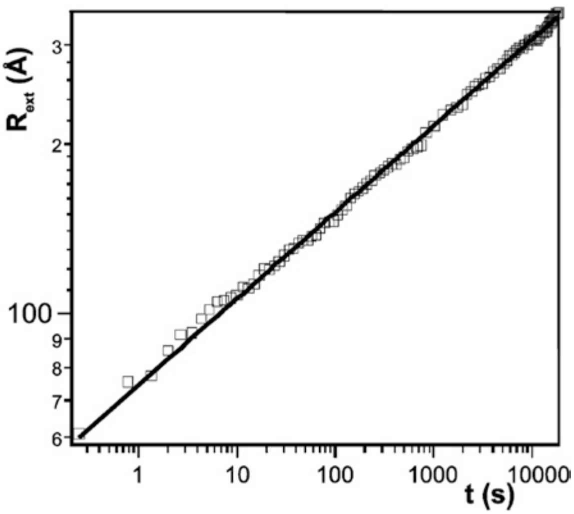

Fig. 5.14 Time-dependence of the vesicle radius in a log–log representation for 0.75 wt. % AOT in 0.042 M NaCl [34]

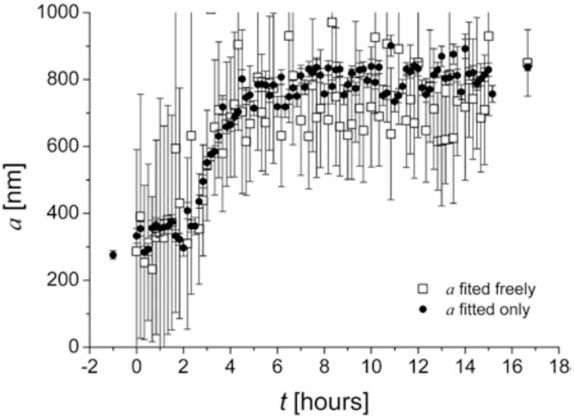

Fig. 5.15 Time dependence of the characteristic length scale for the formation of yogurt as obtained from USANS-experiments [35]

5.4 Stroboscopic Kinetic Experiments

If the time scale of kinetic processes is comparable to or even less than characteristic counting times needed to obtain sufficient statistics, single shot experiments are no longer feasible. In this case, stroboscopic or pump-and-probe techniques can be used where the sample is cycled between to different thermodynamic states. This needs the periodic perturbation of the sample and an appropriate data acquisition system that counts neutron not only as a function of instrument parameters like Q or E but also as a function of time with respect to the perturbation. Time scales down to the microsecond regime are accessible in this way even for real-time inelastic scattering experiments. If the process under consideration is repeatable and the scattered intensity is accumulated over a large number of cycles detailed information about the changes of dynamics and chemical bonding in condensed matter can thus be obtained. Some selected examples of those studies will be presented in the following.

5.4.1 Decomposition Kinetics

It is well known for metallic alloy systems that demixing after thermal heat treatment and subsequent quenching leads to the formation of precipitates that improve the mechanical properties of the material (precipitation hardening). The structure and morphology of precipitates depends on the type of heat treatment and the kinetics of the decomposition process. Two different mechanisms can be distinguished in order to describe the phase separation process: On one hand nucleation and growth is based on the statistical formation of small nuclei that happen to possess the concentration of the product phases. These nuclei then grow in time. Spinodal decomposition, on the other hand, starts from tiny concentration fluctuations that are spatially correlated within the homogeneous phase and grow in amplitude. This mechanism is dominating if the phase separation starts from a thermodynamically unstable state where even small concentration fluctuations are favoured over the homogeneous state. Being a diffusion-limited process, there is a preferred wavelength of growing fluctuations that leads to a correlation peak in the small angle scattering regime. In a second stage, coarsening or Ostwald ripening takes place, associated with an increase of the wavelength and the shift of the correlation peak to smaller wave numbers.

While spinodal decomposition has been studied in some detail in alloys and polymer blends in the past, ionic systems are hardly investigated. Recently, it could be shown, however, that quasi-binary systems of the silver-alkali halide type are almost ideal model systems for detailed investigations of demixing mechanisms and, in particular the competition between nucleation and fluctuations [36–40]. It could be shown, that time resolved diffraction, small angle scattering as well as inelastic scattering from phonons provide complementary information about these systems and allow distinguishing between different aspects on different time-scales. It is observed that the splitting of Bragg reflections due to the difference of the lattice parameters of the product phases is almost independent of the intrinsic chemical demixing process and occurs on a rather long time-scale of hours to months. In contrast, small angle scattering clearly shows the growth of the correlation peaks within minutes. As an example, the evolution of a Bragg reflexion in $Ag_{1-x}Na_xCl$ is shown in Fig. 5.16a after quenching a mixed crystal from the homogeneous phase at 623 K deep into the demixing region below the coherent spinodal line. There is almost no change of the profile even after a few hours apart from wings that are attributed to the concentration modulation [38]. The equilibrium structure with two well

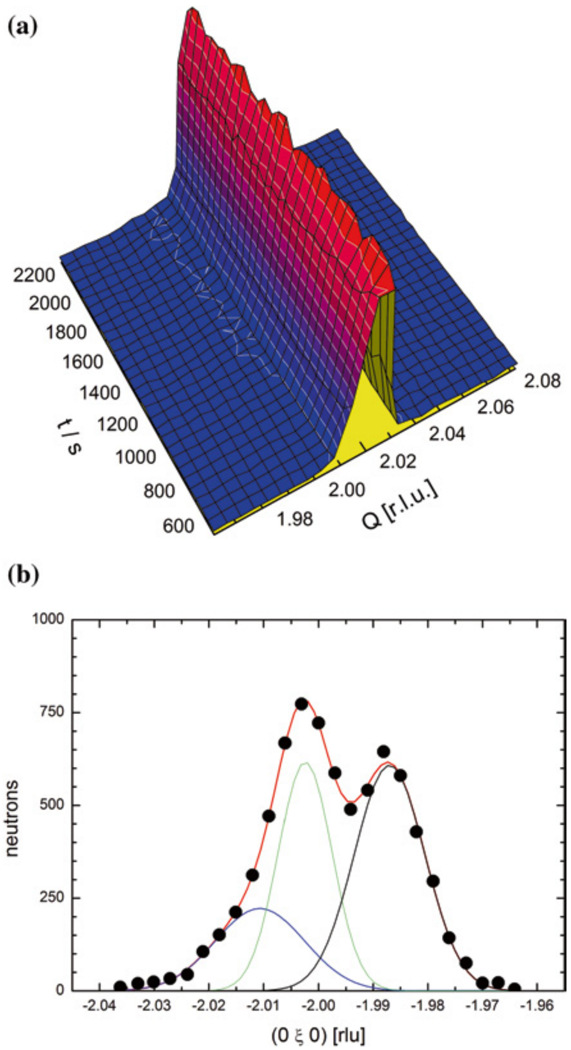

Fig. 5.16 **a** Time evolution of the (200)-Bragg reflexion of $Ag_{0.5}Na_{0.5}Cl$ at 373 K. **b** Bragg profile of a $Ag_{0.4}Na_{0.6}Cl$ single crystal after ageing for more than one year at ambient temperature [39]

separated Bragg peaks for the two product phases is, however, not attained even after months as illustrated in Fig. 5.16b.

The corresponding small angle scattering results are shown in Fig. 5.17 and reveal that the characteristic correlation peak starts to grow within the first few minutes after the quench. Unlike the behaviour of linear systems where the peak position remains constant, in $Ag_{0.5}Na_{0,5}Cl$ the peak is shifted towards smaller Q already at small ageing times.

The inset shows the time-dependence of the peak position: For longer times, the coarsening behaviour Q_{max} proportional to $t^{-1/3}$ according the law of Lifshitz-Slyozov is obtained. Note, that the integrated intensity (in three-dimensional

Fig. 5.17 Time-evolution of the small-angle intensity of $Ag_{0.5}Na_{0.5}Cl$ at 373 K (inset shows the time-dependence of the peak position) [37]

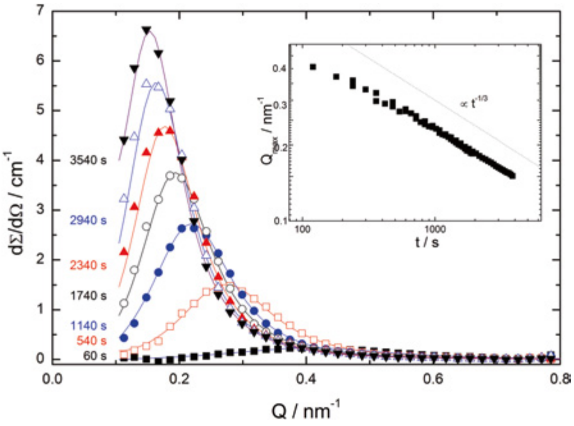

Fig. 5.18 Time-evolution of the TA_1[0.2 0.2 0] phonon in $Ag_{0.45}Na_{0.55}Br$ during demixing at 373 K. The lines are the results of a fit with two Lorentzians, except for the spectrum at t = 45 s which corresponds to the homogeneous state [39]

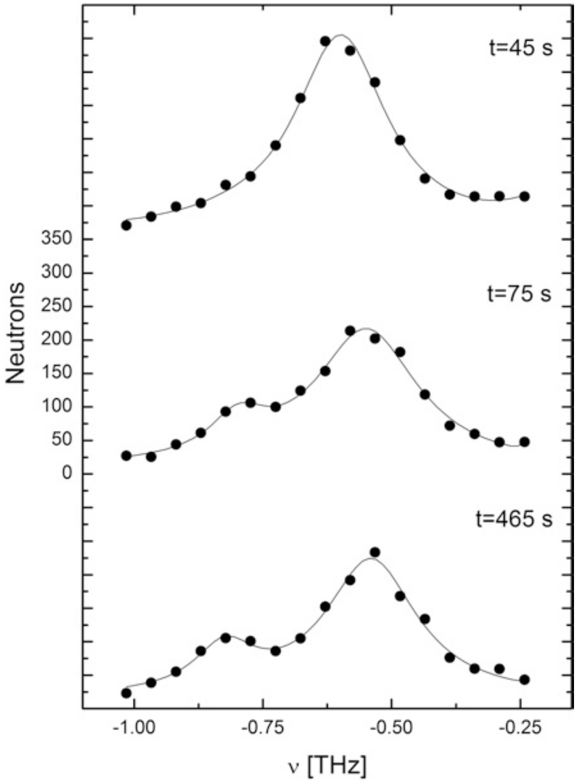

Q-space) is almost constant over the whole time interval proving evidence that the final concentrations are reached already after some minutes.

Inelastic scattering from phonons in single crystals has been used to monitor the variation of the local interionic interactions directly. Due to the

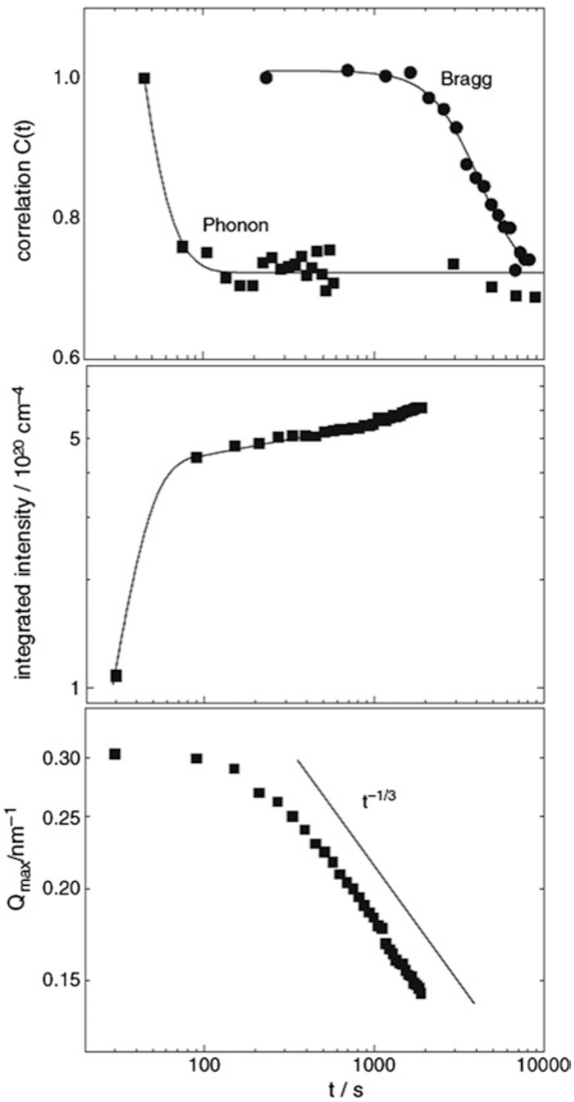

Fig. 5.19 Time-dependence of the autocorrelation function for phonons and Bragg reflections (*top*), integrated small angle intensity (*middle*) and position of correlation peak during demixing at 373 K [39]

different elastic constants of the constituents, acoustic phonons separate into two distinct components during the demixing reaction. For a single crystal with the overall composition $Ag_{0.45}Na_{0.55}Br$, the time-evolution of phonon spectra is shown in Fig. 5.18. It is clearly seen, that the phonons separate within some minutes. This is the most direct proof that the demixing reaction is, in fact, a rather fast process.

The different time-dependent behaviours of Bragg-reflections, phonons, small-angle intensity and correlation peak position are compared in Fig. 5.19 for $Ag_{0.45}Na_{0.55}Br$. It is readily seen that phonons and small angle scattering go hand in hand while the Bragg peaks are delayed. Reason for this behaviour is the existence of coherence strains that keep the lattice almost invariant during the chemical demixing. Only if the precipitates are grown beyond a characteristic size of about 50 nm (as estimated form the position of the correlation peak), the lattice starts to relax giving rise to the splitting of Bragg peaks.

In the corresponding chlorine system, the coherence strains are considerably smaller and so is the driving force for lattice relaxation, which is still not completed after months as shown in Fig. 5.16.

Spinodal phenomena are also observed in crystallization studies of fluoroapatite glass–ceramics. These systems are particularly interesting due to their medical applications and also for opto-electronical applications. It is believed that on cooling cast calcium-fluorapatite glasses are entering a two phase region and an amorphous phase separation takes place leading to a coexistence of a Ca- and F/P-rich phase, on the one hand, and an Al/Si-rich phase, on the other hand, with different glass temperatures. Depending on the initial composition, the phase separation is either dominated by nucleation or spinodal decomposition. In the latter case, the characteristic features of coherent concentration fluctuations can be observed in small angle scattering experiments [41]. On annealing at temperatures close to the respective glass transition temperature, crystallization of the respective phases takes place. This can be monitored by the variation of the small angle intensity profiles as shown in Fig. 5.20.

It can be seen that the correlation peak starts to grow and shifts slightly to smaller momentum transfer. At the same time, the intensity at very small q increases drastically due to the incipient formation of the crystalline phase. At longer ageing times, the correlation peak is completely drowned by the low-q contribution, which seems to saturate after about 800 s. This is an indication that the size of the crystals that can be estimated from the width of the intensity distribution remains in the nanometer regime due to the presence of the second phase that was built during the amorphous phase separation.

It has been pointed out by Hill et al. [41] that the use of neutron techniques is essential for these experiments since they provide the intrinsic bulk behaviour while earlier X-ray data were strongly affected by surface effects. Here, nucleation or phase separation processes may be different to the bulk and, moreover, the surface composition might vary due to the loss of volatile species like silicon tetrafluoride.

5.4.2 Switching Processes In Ferroelectrics and Piezoelectrics

Using stroboscopic thermal neutron diffraction or inelastic scattering, the switching processes or domain redistribution in ferroics under the influence of e.g. pulsed electric fields can be characterized on a microscopic scale. In most cases, the rise time of the electric fields is limiting the time-resolution, due to the inherent capacities present in the sample, leads and plugs. Nevertheless, real-time data in the microsecond-regime could be achieved for several systems.

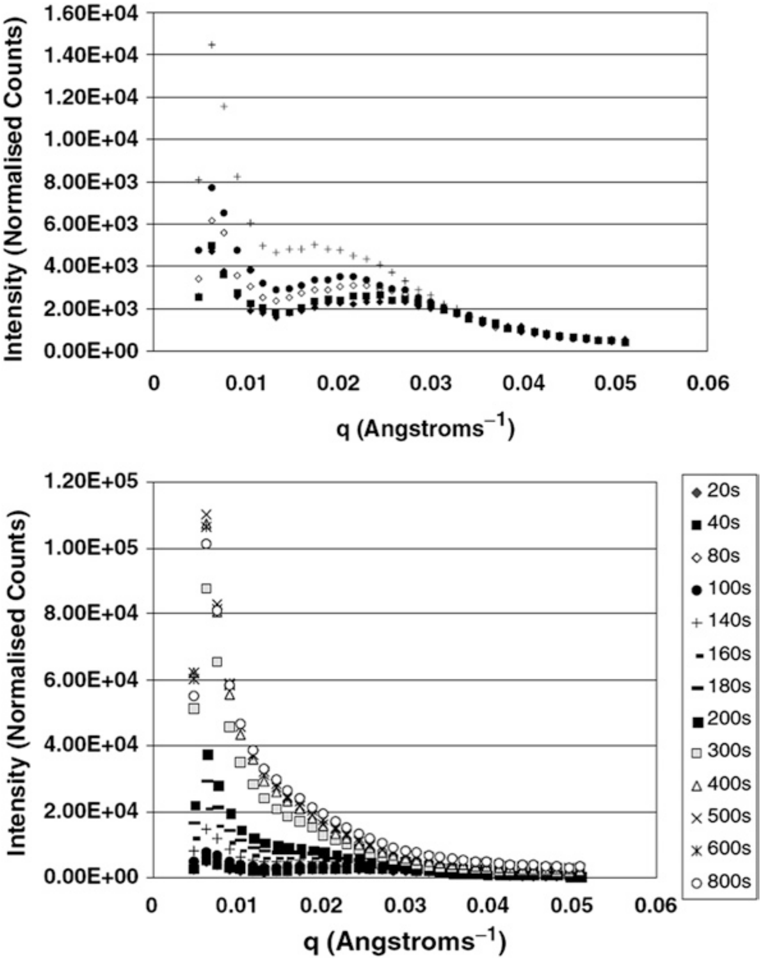

Fig. 5.20 Time-evolution of small angle neutron scattering from a calcium-fluoroapatite glass during annealing at 750 °C [41]

One example is the field-induced polarization inversion in ferroelectric PZN ($PbZr_{1/3}Nb_{2/3}O_3$)–PT ($PbTiO_3$) single crystals. Under zero field conditions, the spontaneous polarization can be oriented along one of the eight (111)—directions of the pseudo-cubic elementary cell. Hence, eight different domains can be distinguished that simultaneously exhibit different piezoelectric strains and slightly different positions of the corresponding Bragg reflections in reciprocal space. Application of an external field will favour one or more of these domains over the others. The redistribution can be monitored by observing the changes of the Bragg-profiles. In Fig. 5.21, selected data are shown for a PZT-PT crystal at different static electric fields as obtained by Daniels et al. [42]. The expected Bragg-positions for the individual domains are marked by black squares.

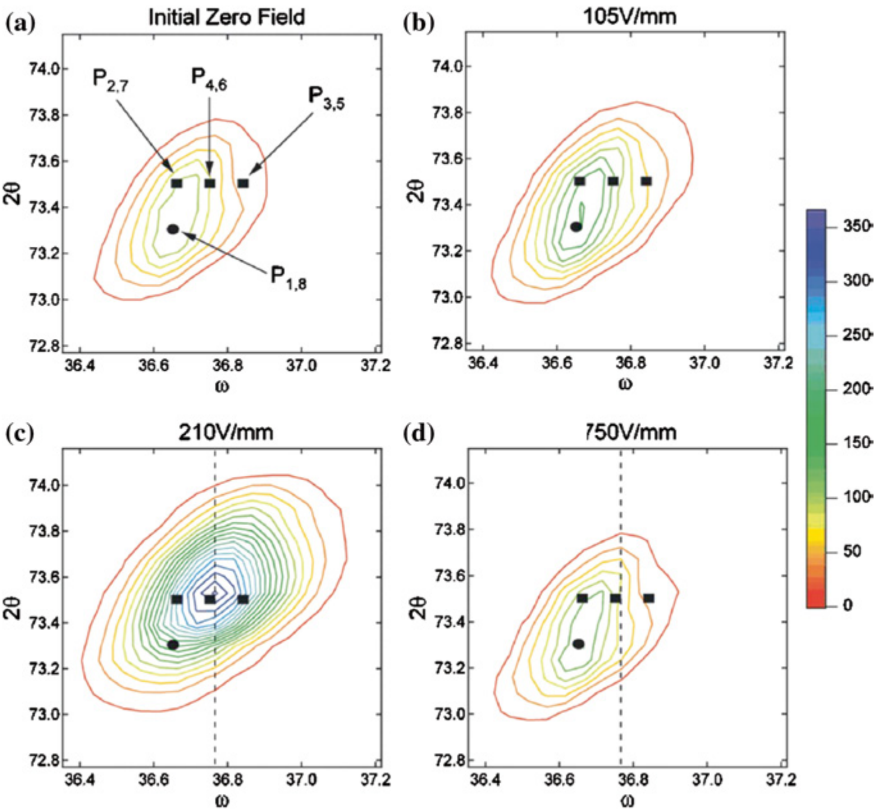

Fig. 5.21 Profiles of the $(222)_c$-Bragg reflection of a PZN-PT single crystal at different electric fields [42]

During polarization reversal under the influence of a bipolar 750 V/mm square wave, the intensity variation was measured at constant crystal orientation along the dashed line. The result is shown in Fig. 5.22. It is clearly seen, that the polarization reversal is associated with an increase of the peak-intensity and occurs almost instantaneously on the time-scale of seconds. There is, however a long time-relaxation with a characteristic decay time of about 5 s leading to a significantly reduced intensity. It is argued that this effect is due to the creep nature of the underlying domain structure [42].

Not only can the domain distribution in ferroelectrics be influenced by an external electric field. Moreover, the ferroelectric transition itself can be induced and its kinetics can be investigated by time-resolved neutron scattering. Modulated ferroelectrics of the A_2BX_4-type (A = K, Rb, NH_4,…, B = Zn, Se, …, X = Cl, Br, O,…) e.g., have been studied in some detail in the past [43–45]. This family of compounds exhibits a variety of modulated phases and the prototypic sequence of phase transitions consists of the high-temperature para-phase, an incommensurate (INC) phase and a low-temperature ordered and sometimes ferroelectric commensurate (C) phase. In this case, the C-phase is stabilised by an electric field and, hence, the lock-in transition

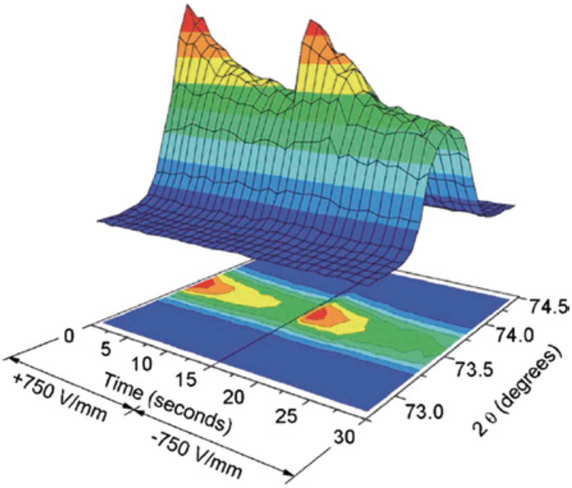

Fig. 5.22 Time evolution of the Bragg-profile during a bipolar square wave of amplitude 750 V/mm and period 30 s [42]

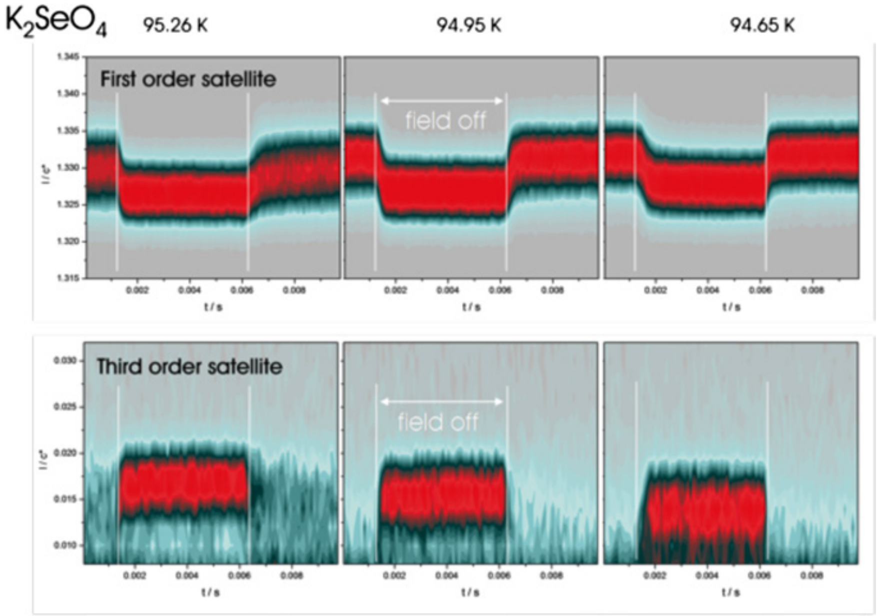

Fig. 5.23 Time-evolution of the first order (*top*) and the third order (*bottom*) satellite patterns in K_2SeO_4 at three temperatures close to the lock-in transition [40]

between the INC and the C-phase may be driven by the external field. The underlying mechanism is governed by the nucleation and growth of topological defects called stripples and antistripples [46, 47]. Details can be studied, if the characteristic satellite reflections are observed experimentally during the transition. For the case of K_2SeO_4, the time-evolution of the intensity maps is shown in Fig. 5.23 not only of the first order satellite (top) but also of the third order one (bottom) for three different temperatures [48].

Since in the C-phase the third order satellite coincides with the fundamental Bragg peak, the switching between the phases is most clearly reflected by the appearance of this new peak when entering the INC-phase. The sequence of temperatures demonstrates that the INC wave vector approaches gradually the commensurate value of 2/3 $\mathbf{c}^*$ on cooling. Careful inspection of the time-evolution of both types of satellites reveals that the relaxation time is considerably temperature dependent. The formation of the ferroelectric phase is delayed by about 200 μs at higher temperatures, while the back-transformation into the INC-phase becomes more sluggish at lower temperatures. The varying thermodynamic driving forces can explain this behaviour.

Even if the phase transitions in K_2SeO_4 are associated with a soft phonon and phason mode, their frequencies close to the lock-in transition are not at all affected by an applied electric field. It is believed that the INC-phase consists of an ordered arrangement of nanometer sized commensurate domains that grow during the (field-induced) lock-in transition. Hence, the local dynamics is already determined by the commensurate structure and independent of the size of domains.

Of particular interest are systems in which the external field is able to affect the balance of interatomic forces, thus inducing softening and a phonon-mediated phase transition. $SrTiO_3$ as a member of the perovskite family is a famous example. Unlike its isotypical counterpart $BaTiO_3$, it does not become ferroelectric even at the lowest temperatures. The transition behaviour is governed by the competition of two soft phonon modes: A zone-boundary phonon becomes soft and on condensation at 105 K, it leads to an antiferrodistortive orthorhombic phase [49]. The zone-centre polar softmode, on the other hand, exhibits an incomplete softening and remains stable down to the lowest temperatures. According to Müller et al. [50], quantum fluctuations prevent its condensation and, hence, the transition to a ferroelectric phase. The application of a sufficiently strong external electric field, however, can induce the ferroelectric order. It has been shown by Eckold [40] that, the softmode itself is altered by the electric field thus leading to a complete softening at the transition and subsequently to a stabilisation within the polar phase. The kinetics of this transition can thus be characterised on a microscopic scale by observing the time-evolution of phonon spectra during the application of pulsed electric fields. Figure 5.24 shows first results obtained with the three-axes spectrometer PUMA at the FRM-II neutron source.

The variation of the inelastically scattered intensity at the Gamma-point (002) is presented (Fig. 5.24a) in the form of a contour plot as a function of frequency and real-time during a 200 Hz pulsed electric field of 8 kV cm^{-1}. Note, that the strong elastic Bragg peak at zero frequency is omitted for clarity. If the field is off, a maximum of the intensity is observed at about 0.75 THz. After switching the field on the maximum is shifted to higher frequencies of about 1 THz as soon as the transition has taken place. As can be seen from the contour plots the phonons are heavily damped. Hence, a careful analysis is needed in order to obtain reliable phonon frequencies. Taking into account the non-linear dispersion of the softmode, contamination from acoustic modes as well as the 4D-resolution function of the three-axes

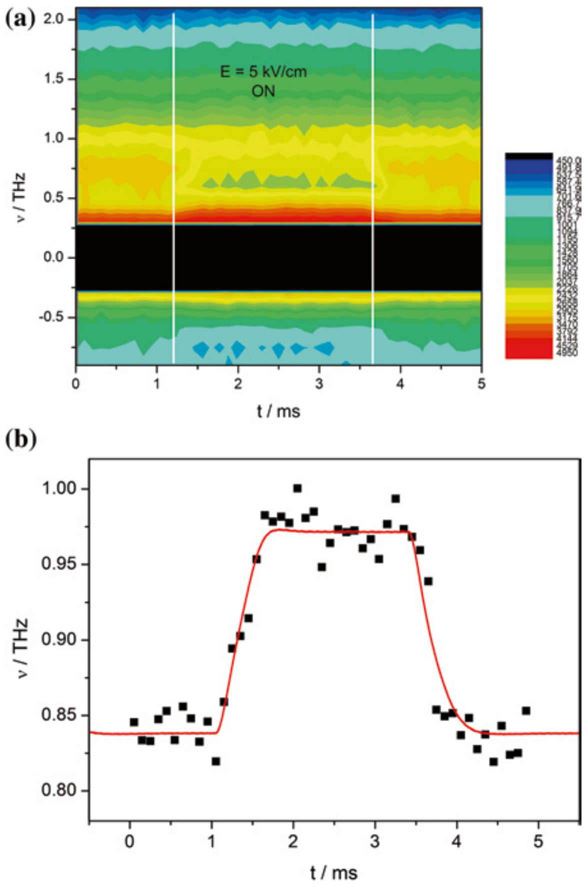

Fig. 5.24 Time evolution of the Γ-point soft-mode in $SrTiO_3$ at 30 K under the influence of a pulsed electric field of 8 kV/cm. **a** Intensity distribution at Q = (2 0 0). Note, that the Bragg-intensity around ν = 0 is omitted. The field is on within the time-interval marked by the vertical lines. **b** Variation of the phonon frequency as obtained by fitting the intensity distribution with a damped harmonic oscillator [40]

spectrometer, we were able to determine the time-dependence of the softmode frequency. The results are shown in Fig. 5.24b. Obviously, the phonon reacts on a time scale of microseconds and seems to follow the applied field instantaneously. Domain walls or other defects do not significantly disturb the dynamical behaviour.

These data show for the first time that it is possible to characterise transformation processes by real-time phonon spectroscopy even on time scales down to microseconds. This technique provides the most direct information about the varying interatomic interactions and chemical bonding.

5.4.3 *Limitations of Stroboscopic Techniques*

There is a principle limitation of the time scales accessible with stroboscopic neutron scattering due to the energy or wavelength distribution of the neutrons. If neutrons with different energies are scattered at a given moment by the sample they will not arrive simultaneously at the detector. Thermal neutrons with typical velocities of 4000 ms^{-1} (wavelength 1 Å) need e.g. 0.5 ms to travel a distance of 2 m between sample and detector. If there is a velocity or wavelength spread of 3 % neutrons that leave the sample simultaneously will be registered in the detector over a time-interval of 15 μs. This gives a lower limit for the attainable time-resolution in kinetic experiments. For cold neutrons this limitation becomes more serious. Typical small angle experiments use neutrons with wavelengths around, say, 5 Å with 10 % bandwidth. If the distance between sample and detector is chosen to be 10 m, the time-resolution becomes worse than 1 ms. In order to overcome this limitation, Wiedenmann et al. have proposed a pulsed beam technique called TISANE [51]. In this approach a chopper placed at a certain distance before the sample generates a bunch of neutrons with a rather large wavelength spread. Neutrons with different wavelengths hit the sample at different times and probe a different state if the sample is perturbed periodically. If scattered elastically, these neutrons can be distinguished by their respective arrival time at the detector. Moreover, the careful synchronization of chopper period, sample perturbation and detector acquisition guarantees that corresponding neutrons of different pulses are always counted in the same time frames of the detector. Hence, neutron counts can be accumulated over a large number of cycles until sufficient statistics is obtained. This method allows accessing time-scales well below 1 ms in small angle experiments even if slow neutrons are employed.

5.4.4 Magnetic Relaxation in Ferrofluids

One of the first examples for the application of this method was the investigation of the structural relaxation of ferrofluids under the influence of AC magnetic fields. Polarized neutrons were used to monitor the spatial orientation distribution of magnetic moments and their variation with the applied magnetic field.

While without any field, the scattered intensity is isotropic and it exhibits a significant angular dependence if a magnetic field is switched on. In Fig. 5.25, the time-dependent intensities scattered from a cobalt-ferrofluid are shown for wave vectors parallel and perpendicular to the applied field. In the upper part of this figure, the results obtained with conventional stroboscopic technique are presented for different frequencies of the applied field. As a reference, the isotropic intensity level for zero field is shown by the dashed line.

Clearly, the time-dependent contrast is almost vanishing at a frequency of 400 Hz. Due to the non-zero wavelength band, the time resolution of this experiment is limited to 1 ms and, hence the signal is averaged over almost half of the period at this frequency. Quantitative analysis has shown that the decay of the signal is not due to the finite mobility of the magnetic moments but simply to the resolution effect.

Application of the TISANE method allows increasing the frequency beyond 1 kHz without restrictions from resolution as shown in the lower part of Fig. 5.25. Here, the intensity modulation is still visible at 1099 Hz and the number of freely oscillating magnetic moments gives its amplitude. At 1424 Hz the scattering contrast

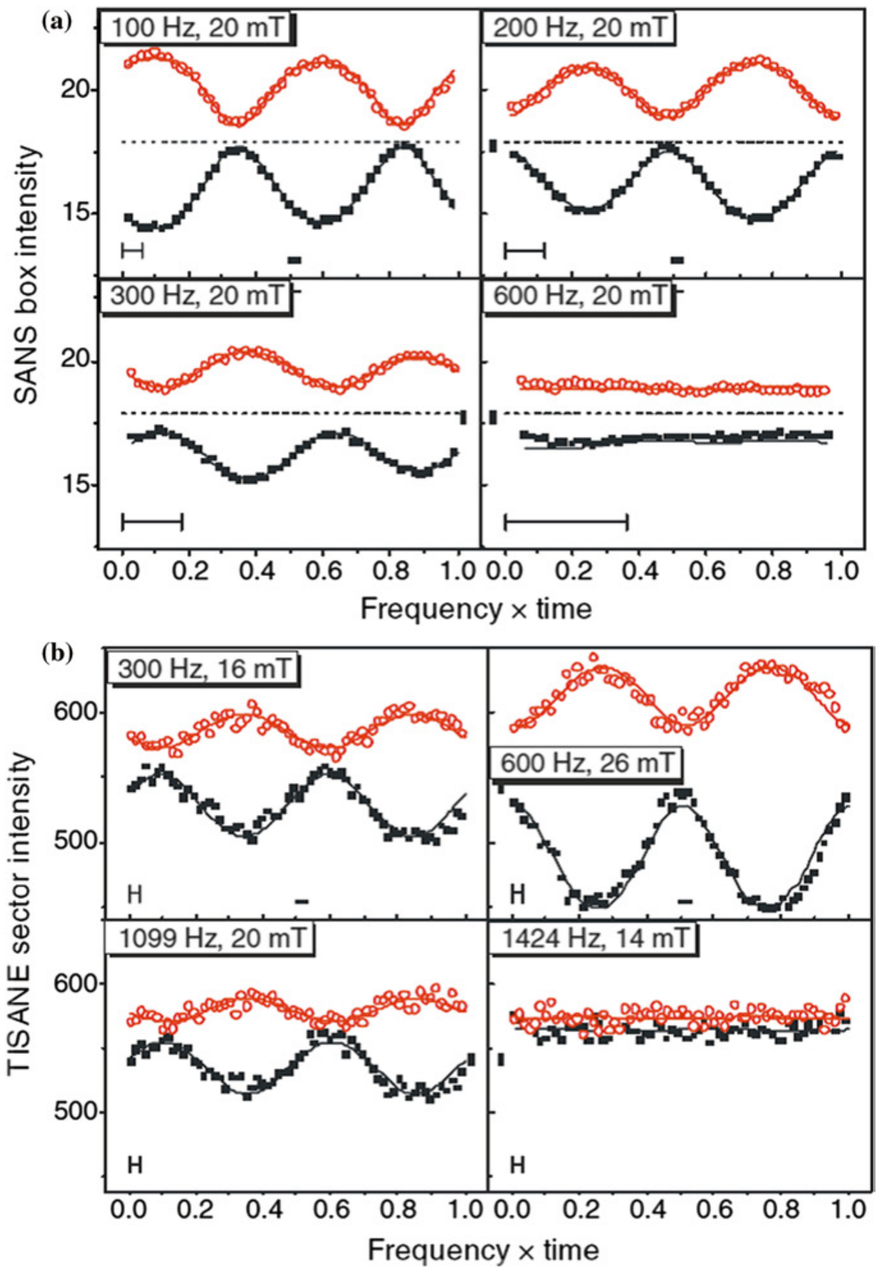

Fig. 5.25 Frequency dependence of scattered intensities from Co-ferrofluid. Bars indicate the experimental resolution. Open (closed) symbols represent the intensity of neutrons scattered into a sector parallel (perpendicular) to the applied field. The *dashed lines* are the results from static SANS experiments without applied field. **a** Stroboscopic SANS mode. **b** TISANE mode. *Solid lines* are the results of fits to a theoretical model [51]

is fading away since the moments are no longer able to follow the external field. Hence, these real-time experiments provide direct information about the relaxation behaviour of the magnetic moments even on time scales well below the millisecond regime.

5.5 Further Prospects of In-situ Investigations

Great progress has been achieved in the field of neutron scattering from materials under extreme or non-equilibrium conditions. Developments for sophisticated sample environment, multiplexing and real-time techniques lead to new fields of application for elastic and inelastic neutron scattering. At different places, instruments are being equipped with user-friendly sample environment. To mention only one specific example: the VULCAN diffractometer at the Spallation Neutron Source SNS in Oak-Ridge focusses on in-situ and real-time experiments for the investigation of the mechanical behaviour of materials [52]. Going one step further many facilities are in the process of setting-up dedicated interface laboratories to allow for more sophisticated experiments by providing extensive off-line preparation and in-situ equipment. Examples are the partnerships for soft condensed matter as well as the extreme conditions initiative at the Institut Laue Langevin in Grenoble, France.

References

1. M. Steiner, J. Low Temp. Phys. **135**, 545 (2004)
2. L. Hennet, S. Krishnan, I. Pozdnyakova, V. Cristiglio, G.J. Cuello, H.E. Fischer, A. Bytchkov, F. Albergamo, D. Zanghi, J.-F. Brun, S. Brassamin, M.-L. Saboungi, Pure Appl. Chem. **79**, 1643 (2007)
3. A. Meyer, S. Stüber, D. Holland-Moritz, O. Heinen, T. Unruh, Phys. Rev. B **77**, 092201 (2008)
4. J. Kozaily, L. Hennet, H.E. Fischer, M. Koza, S. Brassamin, S. Magazù, F. Kargl, Phys. Status Solidi C, 1–4 (2011). doi:10.1002/pssc.201000753
5. S. Klotz, J.M. Besson, G. Hamel, R.J. Nelmes, J.S. Loveday, W.G. Marshall, High Pressure Res. **14**, 249 (1996)
6. Y. Le Godec, M.T. Dove, S.A.T. Redfern, M.G. Tucker, W.G. Marshall, G. Syfosse, S. Klotz, High Pressure Res. **23**, 281 (2003)
7. T. Strässle, S. Klotz, G. Hamel, M.M. Koza, H. Schober, Phys. Rev. Lett. **99**, 175501 (2007)
8. S. Klotz, Th Strässle, A.L. Cornelius, J. Philippe, Th Hansen, Phys. Rev. Lett. **104**, 115501 (2010)
9. Y. Zhao, J. Zhang, H. Xu, K.A. Lokshin, D. He, J. Qian, C. Pantea, L.L. Daemen, S.C. Vogel, Y. Ding, J. Xu, Appl. Phys. A **99**, 585 (2010)
10. E.J. Yearley, L.A. Sasa, C.F. Welch, M.A. Taylor, K.M. Kupcho, R.D. Gilbertdon, R.P. Hjelm, Rev. Sci. Instr. **81**, 045109 (2010)
11. J. Sharma, S. King, L. Bohlin, N. Clarke, Nucl. Instr. Meth. A **620**, 437 (2010)
12. G. Garcés, G. Bruno, A. Wanner, Acta Mater. **55**, 5389 (2007)
13. B. Malard, T. Pirling, K. Inal, E. Patoor, S. Berveiller, Mat. Sci. Forum, Residual Stresses VII, **524–525**, 905 (2006)
14. C.D.M. Liljedahl, O. Zanellato, M.E. Fitzpatrick, J. Lin, L. Edwards, J. Fatigue **32**, 735 (2010)

15. W. Woo, Z. Feng, X.L. Wang, D.W. Brown, B. Clausen, K. An, H. Choo, C.R. Hubbard, S.A. David, Sci. Technol. weld. **12**, 298 (2007)
16. P. Smeibidl, A. Tennant, H. Ehmler, M. Bird, J. Low Temp. Phys. **159**, 402 (2010)
17. S. Yoshii, K. Ohoyama, K. Kurosawa, H. Nojiri, M. Matsuda, P. Frings, F. Duc, B. Vignolle, G.L.J.A. Rikken, L.-P. Regnault, S. Michimura, F. Iga, Phys. Rev. Lett. **103**, 077203 (2009)
18. R. Le Toquin, W. Paulus, A. Cousson, C. Prestipino, C. Lamberti, J. Am. Chem. Soc. **128**, 13161 (2006)
19. http://www.helmholtz-berlin.de/user/neutrons/instrumentation/laboratories/degas/index_en.html
20. V.K. Peterson, C.M. Brown, R.A. Livingston, Chem. Phys. **326**, 381 (2006)
21. V.K. Peterson, in *Studying kinetics with neutrons* ed. by G. Eckold, H. Schober, S.E. Nagler. Springer Series in Solid State Physics, vol 161 (Springer, Berlin, 2010), p. 19
22. V.K. Peterson, A.E. Whitten, J. Phys. Chem. C **113**, 2347 (2009)
23. V.K. Peterson, D.A. Neumann, R.A. Livingston, Chem. Phys. Lett. **419**, 16 (2006)
24. V.K. Peterson, M.C.G. Juenger, Phys. B **385**, 222 (2006)
25. C.G. Salzmann, P.G. Radaelli, E. Mayer, J.L. Finney, Phys. Rev. Letters **103**, 105701 (2009)
26. T.C. Hansen, M.M. Koza, P. Lindner, W.F. Kuhs, J. Phys. Condens. Matter **20**, 285105 (2008)
27. M. Koza, T. Hansen, R.P. May, H. Schober, in *Studying Kinetics with Neutrons* ed. by G. Eckold, H. Schober, S.E. Nagler. Springer Series in Solid State Physics, vol 161 (Springer, Berlin, 2010), p. 77
28. D. Ma, A.D. Stoica, X.L. Wang, Z.P. Lu, T. Proffen, Appl. Phys. A **99**, 537 (2010)
29. F. Xia, Q. Gujie, J. Brugger, A. Studer, S. Olsen, A. Pring, Rev. Sci. Instr. **81**, 105107 (2010)
30. C.R. Haramagatti, A. Islamov, H. Gibhardt, N. Gorski, A. Kuklin, G. Eckold, PCCP **8**, 994 (2006)
31. R. Lund, in *Studying Kinetics with Neutrons* ed. by G. Eckold, H. Schober, S.E. Nagler. Springer Series in Solid State Physics, vol 161 (Springer, Berlin, 2010), p. 213
32. R. Lund, L. Willner, J. Stellbrink, P. Lindner, D. Richter, Phys. Rev. Letters **96**, 068302 (2006)
33. A. Halperin, S. Alexander, Macromolecules **22**, 2403 (1989)
34. I. Grillo, E.I. Kats, A.R. Muratov, Langmuir **19**, 4573 (2003)
35. L.F. van Heijkamp, I.M. de Schepper, M. Strobl, R.H. Tromp, J.R. Heringa, W.G. Bouwman, J. Chem. Phys. A **114**, 2412 (2010)
36. G. Eckold, J. Phys. Condens. Matter **13**, 217 (2001)
37. D. Caspary, G. Eckold, F. Güthoff, W. Pyckhout-Hintzen, J. Phys. Condens. Matter **13**, 11521 (2001)
38. G. Eckold, D. Caspary, H. Gibhardt, W. Schmidt, A. Hoser, J. Phys. Condens. Matter **16**, 5945 (2004)
39. P. Elter, G. Eckold, H. Gibhardt, W. Schmidt, A. Hoser, J. Phys. Condens. Matter **17**, 6559 (2005)
40. G. Eckold, in *Studying Kinetics with Neutrons* ed. by G. Eckold, H. Schober, S.E. Nagler. Springer Series in Solid State Physics. vol 161 (Springer, Berlin, 2010), p. 178
41. R. Hill, A. Calver, A. Stamboulis, N. Bubb, J. Am. Ceram. Soc. **90**, 763 (2007)
42. J.E. Daniels, T.R. Finlayson, M. Davis, D. Damjanovic, A.J. Studer, M. Hoffmann, J.L. Jones, J. Appl. Phys. **101**, 104108 (2007)
43. G. Eckold, H. Gibhardt, D. Caspary, P. Elter, K. Elisbihani, Z. Krist. **218**, 154 (2003)
44. G. Eckold, M. Hagen, U. Steigenberger, Phase Transitions **67**, 219–245 (1998)
45. K. Elisbihani, H. Gibhardt, G. Eckold, Phys. Chem. Chem. Phys. **11**, 3168–3175 (2009)
46. V. Janovec, Phys. Lett. **99A**, 384 (1983)
47. K. Kawasaki, J. Phys. C Solid State Phys. **16**, 6911 (1983)
48. J. Leist, Thesis, University of Göttingen, 2008
49. G. Shirane, Y. Yamada, Phys. Rev. **117**, 858 (1969)
50. K.A. Müller, H. Burkard, Phys. Rev. B **19**, 3593 (1979)
51. A. Wiedenmann, U. Keiderling, K. Habicht, M. Russina, R. Gähler, Phys. Rev. Letters **97**, 057202 (2006)
52. P.K. Liaw, H. Choo, R.A. Buchanan, C.R. Hubbard, X.L. Wang, Mat. Sci. Eng. A **437**, 126 (2006)